Measurement of Aerodynamically Induced Blade Distortion on a Shrouded Counter-Rotating Prop-Fan

J. Klinner[1,*], M. Schroll[1,*], T. Lengyel-Kampmann[2], J. Belz[3], F. Eichner[3], P. Winkelmann[4], C. Willert[1]

1: Institute of Propulsion Technology (Measurement Techniques), German Aerospace Center (DLR), Köln, Germany
2: Institute of Propulsion Technology (Fan and Compressor), German Aerospace Center (DLR), Köln, Germany
3: Institute of Aeroelastics (Aeroelastic Experiments), German Aerospace Center (DLR), Göttingen, Germany
4: Institute of Structures and Design (Component Design and Manufacturing Technologies), German Aerospace Center (DLR), Stuttgart, Germany
*Corresponding author: joachim.klinner@dlr.de

Keywords: blade deformation, pulsed high-power LED illumination, image pattern correlation technique, IPCT, boundary layer ingestion, BLI, counter-rotating fan

ABSTRACT

Blade deformation on a 1 m diameter composite fan rotor is measured simultaneously using stereoscopic image pattern correlation technique (IPCT) and blade-tip imaging. Absolute referencing of the blades is made possible by simultaneously tracking a marker on the hub using a fourth camera. Illumination is provided by microsecond pulses of high-power LEDs. Rise and fall time in the 100 ns regime are achieved using a self-designed high-current drive circuit. A high-speed microcontroller provides accurate, speed-independent angular delays to enable phase-locked triggering of cameras and LEDs. Mean and RMS deformation of the blade are acquired for different aerodynamic loading conditions induced by imposing a non-uniformity upstream of the rotor aimed at mimicking boundary layer ingestion.

1. Introduction

The work was performed within the DLR internal project AGATA3S which focusses on the interaction of a counter-rotating shrouded propfan with a distorted incoming flow as expected for fuselage integrated engines, also referred to as boundary layer ingestion (BLI). For this purpose a dedicated counter-rotating shrouded fan stage (CRISP2) was specifically designed, manufactured and commissioned by the end of 2021 (Aulich et al., 2013; Schmid et al., 2019; Lengyel-Kampmann et al., 2022). The material presented herein describes the design and implementation of the optical instrumentation required to realise blade deformation measurements based on the image pattern correlation technique (IPCT) in a stereoscopic imaging configuration. In the process, a microcontroller-based synchronization system was specifically designed to provide phase-locked trigger signals for pulsed illumination and cameras. Furthermore, modifications of current drivers

for high-power LED (HP-LED) resulted in significant improvement of the luminosity rise time such that “sharp" pulses of light can be produced in the one-microsecond range. This allows the capture of crisp images of the blades that rotate with tip speeds up to 260 m/s at aerodynamic design point (ADP). The IPCT data ultimately provides snap-shot data of the blades’ dynamic deformation, in particular, the blades’ deflection, torsion and higher orders of flexure and will be compared to numerical predictions.

2. Experimental Setup and Methods

2.1. Test facility and fan rig

The counter-rotating fan rig is mounted in the two-spool test facility M2VP of the Institute of Propulsion Technology of the German Aerospace Center (DLR). The assembled rig is shown in Fig. 1. In the background the two 5 MW motors can be seen. The CRISP2 rig consists of 10 blades in the front rotor (R1) and 12 blades in the downstream rotor (R2) with a diameter of about 1000 mm. The blades of the rotors are made of composite material and designed to rotate in a 10-to-8 speed ratio. The rig operating conditions are summarized in 1. At 100% rotational speed (working line) the rig reaches a reduced mass flow of 156 kg/s with blade tip speeds exceeding 260 m/s at flow Mach numbers at the tip of Ma = 1. The incoming fuselage boundary layer is simulated using a boundary layer fence followed by a honeycomb flow straightener about 3 m upstream of the fan. The boundary layer fence, shown in Fig. 3, can be hydraulically put into position at different depths and is fully rotatable around the perimeter such that the instrumentation can measure the distortion effects without needing to be traversed.

A schematic of the rig is provided in Fig. 2. It is extensively instrumented with dynamic and static pressure measurement probes, rakes for pressure/temperature traverses as well as access ports forhotwire anemometry (HWA) and both planar and curved windows for particle image velocimetry (PIV) and image based deformation measurement techniques. The blades themselves are equipped with strain gauges, unsteady pressure measurement (Kulite) and are additionally monitored with a blade tip timing measurement system (BSSM) provided by MTU.

Table 1. CRISP2 operating conditions.

	ADP	Cruise	Cutback	Approach	
fan pressure ratio	1.3	1.2780	1.1945	1.0830	
isentropic efficiency	0.9323	0.9171	0.9021	0.8821	
mass flow, $\dot{m}$	159.0	155.2	136.7	96,8	kg/s
rotor R1 speed	5044	4920	4290	2989	rpm
R1 relative speed	100	97.5	85.0	59.3	%
R1 tip speed	262.5	256.0	223.3	155.6	m/s
R1 tip Mach number	1.048	1.022	0.858	0.575	m/s

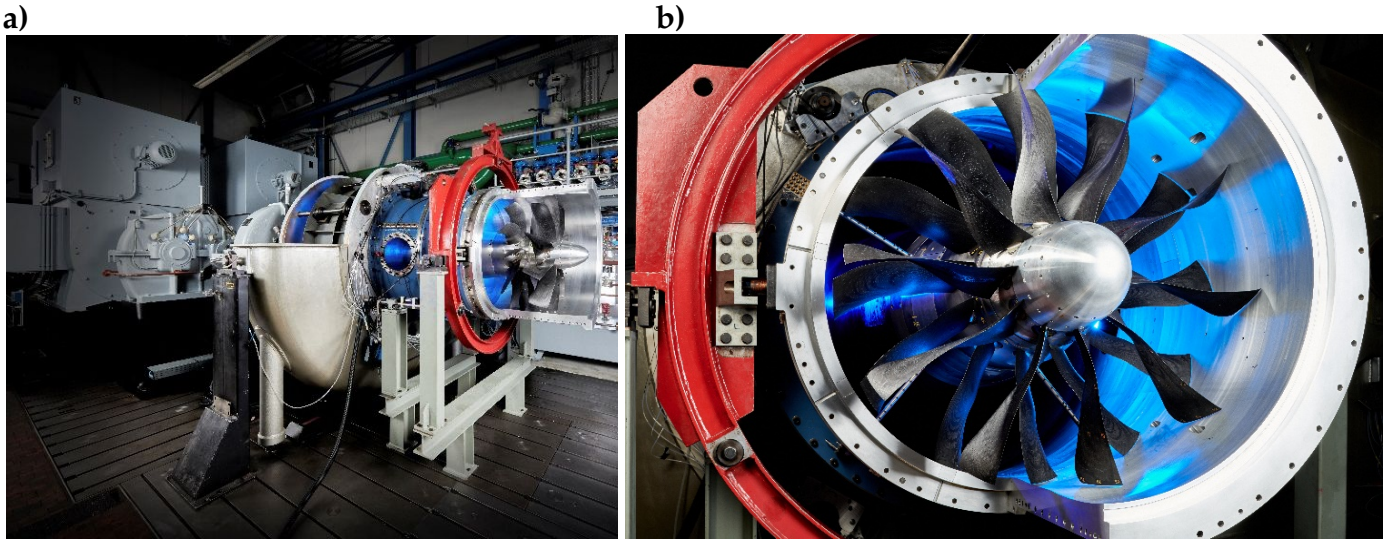

Figure 1. Photograph of the two-spool test facility (M2VP) with the mounted CRISP2 propfan (casing partially removed).

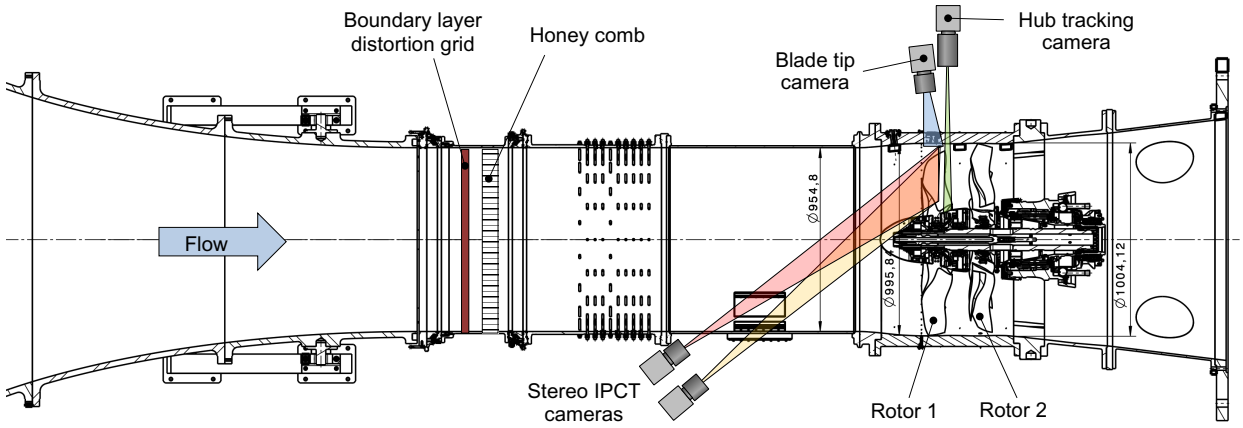

Figure 2. Overview of the IPCT instrumentation on the CRISP2 rig.

2.2. IPCT instrumentation

For optical blade deformation measurement, the IPCT is used in a stereoscopic configuration (Boden & Stasicki, 2014; Kirmse et al., 2016; Meyer et al., 2014). This is realized by coating the blades with a fixed random dot pattern that is imaged with high resolution cameras. Correlation-based processing of the recorded stereo image pairs provide disparity maps that are mapped onto the blade geometry to estimate the blade's deflection. Reference markers on the blade are used to align the measured data with the corresponding CAD geometry of the blade. In the present setup the types of random patterns are applied to the blades (c.f. Fig. 13b). The first type is based on discrete random white dots of about 2 mm diameter that are created by spray-painting a removable perforated mask. The other pattern is created by coating the blade surface with retro-reflective paint which consists of small glass beads of $\approx 100-300\,\mu m$ diameter embedded in clear acrylic paint.

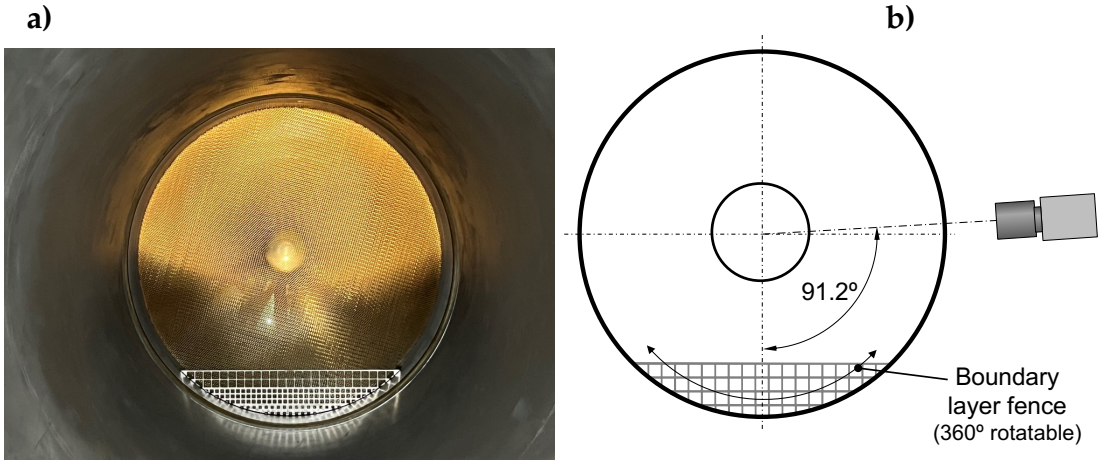

Figure 3. Boundary layer fence used to introduce an incoming flow distortion to mimic the fuselage boundary layer of an aircraft. It is positioned about 3 m upstream of the fan stage and fully rotatable around the circumference.

2.3. Displacement accuracies from mockup experiment

The achievable accuracies for static 3c deformations of the blade's surface were determined in advance through a mockup experiment that duplicates the stereoscopic camera arrangement and imaging conditions (i.e. working distances of ≈ 1300 mm). For this purpose, a flat plate of 160×800 mm^2 was painted with different patterns and imaged with different imposed displacements both in the circumferential direction (y-axis) as well as perpendicular to the outer chord of the blade (z-axis). Random dot patterns involved different marker sizes (white spots on a dark background) and sprayable retro-reflective paint, consisting of small glass beads embedded in acrylic paint. Using linear stages, the dot patterns were displaced successively in 50 µ steps up to 0.5 mm along the two axes. IPCT images were acquired with both pulsed laser and pulsed LED illumination.

Displacements were calculated from three planar displacement fields obtained from cross-correlation between four dewarped images (two camera views, both reference and displaced images), all initially dewarped onto the same calibration target. The 3d reference position of the speckle pattern ("cold position") was triangulated based on the disparity map between non-displaced camera views and the two camera positions estimated using the Tsai camera model (Tsai, 1987; Willert, 2006). Combined with cross-correlations of the images at the reference and displaced positions from both cameras, the full 3c displacement vector was recovered for each interrogation window.

Fig. 4 shows representative interrogation windows and 2d cross-correlations of dewarped patterns of random white dots and of retro-reflective paint. As to be expected, illumination of the dot patterns with a coherent light source, here a frequency doubled Nd:Yag pulsed laser (pulse width=8 ns) resulted in significant speckle effect in the form of high spatial frequency modulations (statistical interference patterns on rough surfaces) that propagate into the cross-correlation maps. These specular patterns are mitigated through the use of a broadband light source such as an LED and results in smooth signal peaks in the correlation map, their size proportional to the marker size. In combination with the retro-reflective microspheres, the correlation peak narrows down

considerably. For the dot patterns a parameter optimization for sub-pixel position estimation of the correlation maximum gave best results using a non-linear Gaussian fit over 5 pixels. The correlation maps of the microspheres were optimally processed using truncated sinc peak fit (Roesgen, 2003). Fig. 5 provides an overview of the deviations from the target displacements of the stage for each combination and clearly highlight the advantage of the retro-reflective surface coating in terms of standard deviation over all vectors evaluated in the planar field. For a final window size of 5.2×5.2 mm^2 (64×64 pixels) the mean standard deviation of all targeted displacements in chord-normal direction reduces by a factor of 1.94 using LED illumination instead of coherent light to illuminate 2 mm dots, and further decreases by a factor of 1.88 when retro-reflective paint is used instead of dots. Based on this investigation, the actual measurements on the rig were performed using LED illumination and retro-reflective microspheres. Dot markers were additionally applied onto a separate blade as a fall-back option.

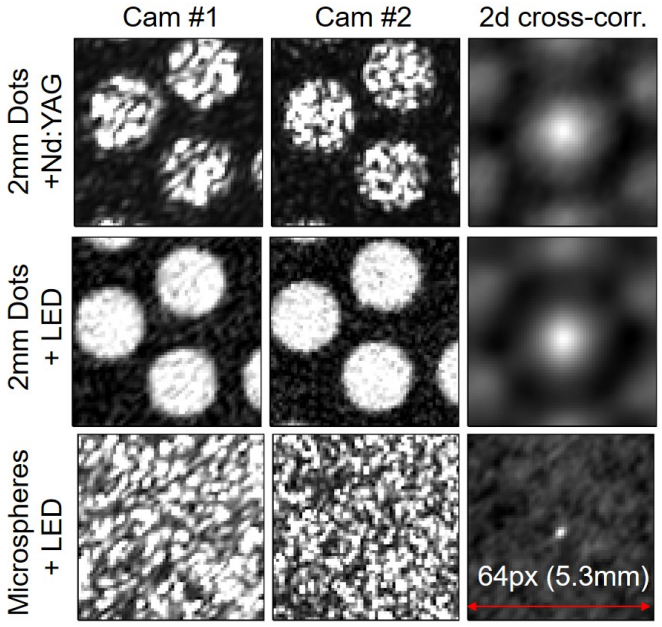

Figure 4. Dewarped image patches of 64×64 pixels of discrete random white dots of about 2 mm diameter (top,middle) and of microspheres (bottom) recorded with the stereoscopic IPCT camera arrangement (c.f. Fig. 13) during mockup experiments.

2.3.1. Pulsed LED illumination

Given a rotation speed of up to 5200 rpm the blades exhibit a tip velocity of up to 270 m/s (or 270 µm/µs) such that flash-based illumination (or camera shutter) in the single microsecond range is required to keep motion blur acceptable, that is, within a few pixels on the image detector. Preliminary studies ruled out the use of flash lamp pumped pulsed lasers, mostly due to the speckle artifacts they introduce and their need for fixed-frequency operation that makes phase-locked measurements challenging. In addition a minimum of 2 laser systems would be required illuminate the scenes imaged by 4 cameras at different viewing directions. Instead, pulsed illumination was realized using cost-effective HP-LEDs operated with high-current pulsing (Willert et al., 2010). To

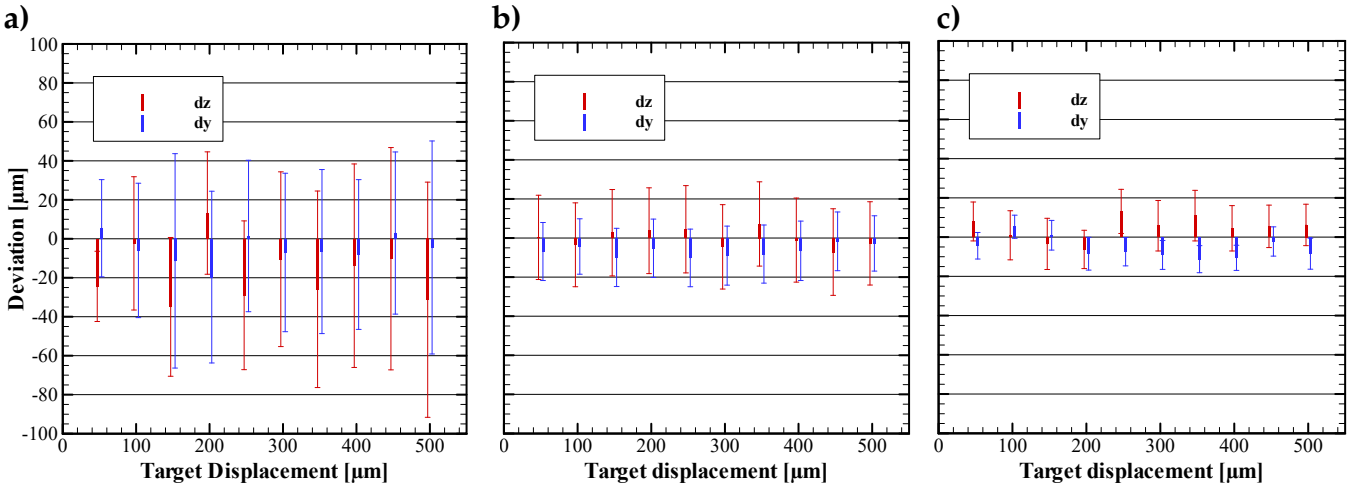

Figure 5. Deviation from target displacements in circumferential direction y and normal to the outer chord z for different patterns and illumination types for the stereoscopic camera arrangement (c.f. Fig. 13); a) Nd:Yag laser and dots of 2 mm dia.; b) LED and dots of 2 mm dia. c) LED and retro-reflective paint. Error bars represent $\pm 2\sigma$ of 86×39 vectors evaluated by a multigrid approach with final interrogation window size of 5.2×5.2 mm^2 (64×64 pixels) in a planar region of 160×800 mm^2.

further overcome the slow rise time of O(500ns) of the HP-LED's emission, the rise time was reduced through modifications of the driving circuit originally presented by Willert et al. (2010) as shown in Fig. 6. Pulse shaping is possible by adding a combination of a small resistance R_p and capacitance C_p in series with the LED as suggested by Halbritter et al. (2014). By choosing $R_p = 0.5\,\Omega$ and $C_p = 200$ nF the rise time of the LED's luminosity can be reduced from $\tau_{rise} \approx 840$ ns in the original design to $\tau_{rise} \approx 170$ ns (c.f. Figure 7, right). The modified circuit initially drives the LED with a significantly higher current (factor 2-3$\times$) for a short duration determined by the capacitance C_p and thereby results in a faster rise time of the LED's luminosity. The ratio between the steady and the over-peaking current is determined by R_p and the LED's internal resistance R_{LED}. Compared to the light pulse produced by the original driver design the shape of light pulse is nearly symmetric for a pulse duration of 1 µs.

For the experiments four separate HP-LEDs were driven at a peak current of $I_{f,\mathrm{max}} \approx 120$ A that levels out at $I_f \approx 50$ A after about 500 ns for the remainder of the pulse. The LED (OSRAM LE CG P2A) is specified for a constant current of $I_f = 20$ A and a surge current of $I_f = 42$ A for durations up to $t_p = 10$ µs and duty cycles of $D = 10\%$. Here, the surge current is exceeded by a factor of 3 whereas the duty cycle is three orders of magnitude smaller: $D = 1$ µs $\times$ 100 Hz $= 0.01\%$.

Table 2 summarizes the specifications of several HP-LED singled out for possible use. The devices from OSRAM were actually available for the study; the specifications of Luminus devices are from respective data sheets. Most of the devices use phosphor converted green emitters with a wide spectral bandwidth of 100 nm and share a common emission angle 120°. On this basis the relevant figure for choosing the LED is the luminance per unit area $\Phi_v / A_{\mathrm{LED}}$ that is maximized for the OSRAM LE-CG-P3A.

Table 2. HP-LED specifications.

Model		LE-CG-P2A	LE-CG-P3A	PT121-G	CFT90-CG	
Manufacturer		OSRAM	OSRAM	Luminus	Luminus	
luminance, min.	$\Phi_{v,\mathrm{min}}$	8421	10645		6200	lm
luminance, max.	$\Phi_{v,\mathrm{max}}$	8725	11119		10750	lm
luminance, typ.	$\Phi_{v,\mathrm{typ}}$	8570	**10885**	5200	8500	lm
emitting area	A_{LED}	3.23×2.55	4.8×2.6	4×3	3×3	mm^2
mean luminance per area	Φ_v/A_{LED}	**1041**	872	433	942	$\mathrm{lm}\cdot\mathrm{mm}^{-2}$
drive current	I_f	24	36	30	22.5	A
pulsed current	$I_{f,p}$	32	48	36		A
surge current (<10µs)	$I_{f,s}$	42	60	42	36	A
peak wavelength	λ_{peak}	520	520	525	580	nm
spectral bandwidth	$\Delta\lambda$	100	100	34	103	nm
viewing angle at 50%	2φ	120°	120°	(120°)	120°	

2.3.2. Phase-locked measurement technique

A further challenge in acquiring adequate IPCT recordings from the rotating propfan is a speed-independent, stationary phase (angle) trigger to initiate image capture and pulse the HP-LEDs. This is accomplished with a microcontroller (PJRC Teensy 4.1) operating at 600 MHz that continuously measures the period provided by the 1/rev trigger of the rotor spindle. Based on this period, appropriate delays are calculated on the fly to trigger both the cameras and the HP-LEDs. Under ideal conditions, that is, with a constant frequency trigger source of about 100 Hz, the jitter on the phase-shifting delay is on the order of ± 3 ns. Using a 10-bit, high-speed oscilloscope (Rohde&Schwarz RTB2004, 300MHz, 2.5GS/s) measurements of the phase delay obtained from the rig at a speed-line of 85% reveal a relative angular uncertainty on the order of $2{\cdot}10^{-4}$ for shift angles greater than 10°. A constant offset of ≈0.17° (6.5 µs) could be observed for all set-angles and is due to internal signal processing by the microcontroller. In spite of the trigger stability, a jitter of the trigger of ± 3 µs (about $0.1°$) could be observed during the initial IPCT measurements, possibly due to continuous variations in the rotor speed or electro-magnetic interference issues. To account for this additional uncertainty a reference marker placed on the hub of rotor no.1 was imaged by a fourth sCMOS camera (see Fig. 10c). The reference marker, a random dot pattern attached to the hub, was stroboscopically illuminated by an additional HP-LED.

3. Results

3.1. Rig commissioning and instrumentation test

Phase-stationary triggering of HP-LEDs and cameras could be tested in the process of commissioning the CRISP2 test rig by imaging the blade tip through a casing window with matching inner contour. Figure 9 shows a composite image obtained by combining snapshots recorded by a sCMOS camera (ILA.PIV.sCMOS, 2540×2048 pixel). The blade tip has white markers painted on it

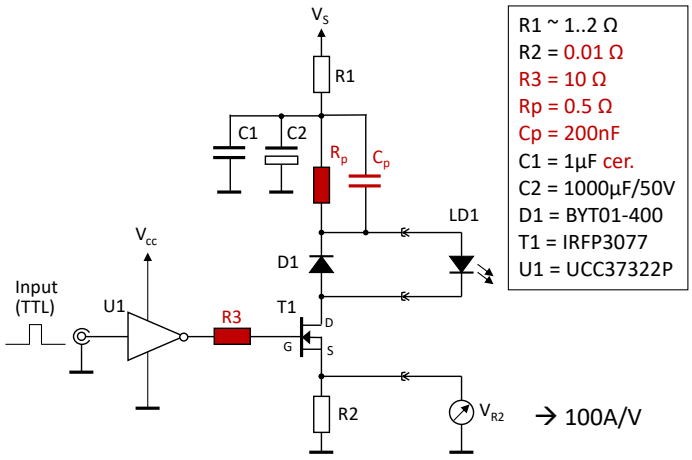

Figure 6. LED driver circuit based on the design presented in Willert et al. (2010) with modifications indicated by components in red.

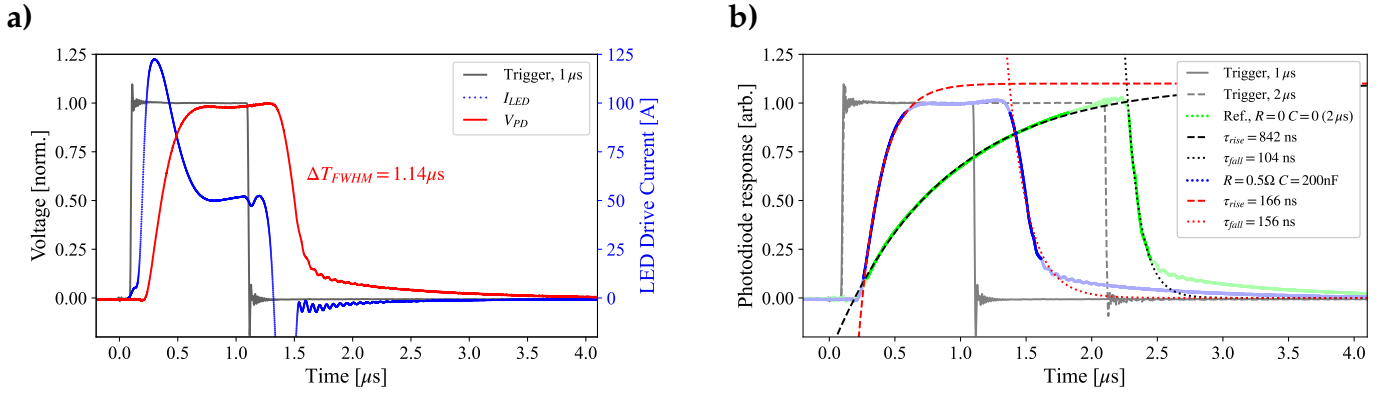

Figure 7. left: LED luminosity (red) as a function of time when driven by a 1 μs current pulse (blue) using the circuit shown in Fig. 6. Right: comparison of LED luminosity between original (green) and modified design (blue).

to be able to track the blade's position. The HP-LED (OSRAM OSTAR LE-CG-P2A) is driven with a 100 A current of 1 µs duration as shown in Fig. 7.

The composite image of Fig. 9 shows an average of the marker positions obtained from 500 images at 15% of the rig's design point. The slight blur of the markers is due to frame-to-frame jitter of about 3 µs combined with blade vibration. The image of the offset markers represents a single snapshot acquired at 42% speed and shows no noticeable motion blur due to the short illumination pulse. During 1 µs the blade translates by about 100 µm. The offset of the markers at 42% with respect to the reference speed of 15% reflects the increased aerodynamic loading of the blade along with systemic effects such as bearing play and constant offsets introduced by the phase-stationary triggering.

Figure 9c provides an estimate of the blade's axial displacement when increasing the rotor speed from 15% to 38%. The variation of the displacement along the blade's chord reflects the blade's torsion under aerodynamic and centrifugal loading. At this point further analysis is hampered due to the fact that data of the exact position of the rotor hub was not available.

The initial measurements acquired in the course of the rig's commissioning also confirmed that the

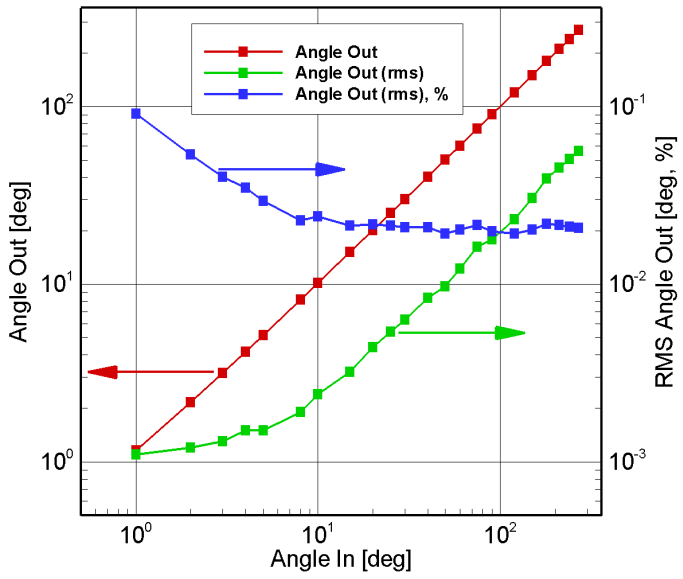

Figure 8. Performance of phase shifter for different preset angles obtained at speed-line 85% with a spindle speed of 4310 rpm (71.9 Hz).

HP-LEDs provide sufficient light to adequately image the rotating IPCT markers for both types of surface coating.

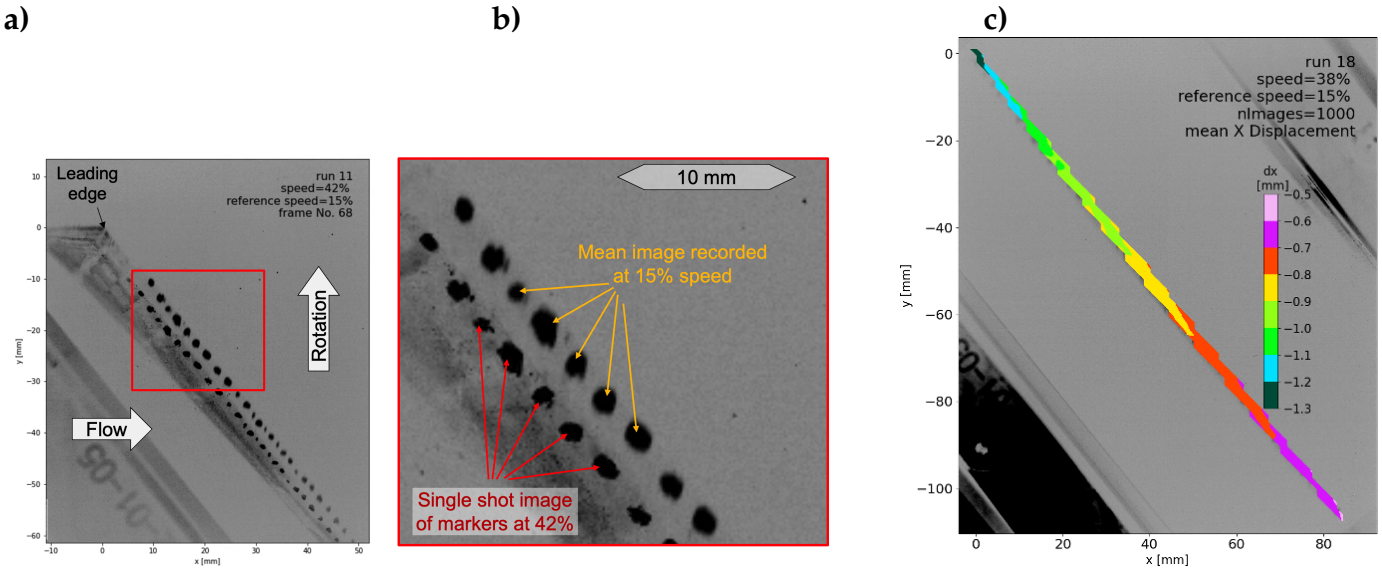

Figure 9. Preliminary recording of the blade tip's displacement at the 42% speed-line with respect to 15% (reference condition). The flow is from left to right; blade movement is upwards.

3.2. Measurement campaign

For the actual measurements a fourth camera was added to image a reference marker on the hub of rotor 1 in order to account for the frame-to-frame jitter observed during the commissioning phase. To achieve focussed images the larger contoured window was replaced by two small circular windows of about 50 mm clear aperture (Fig. 10a). As a consequence only a portion of the 135 mm chord length of the blade tip is visible, ruling out reliable measurements of the blade's

torsion alongside with its deflection. Sample images recorded at the 40% speed line are provided in sub-figures 10b and 10c. To enhance detection accuracy of tip displacements, the blade tip was painted with both small dots and retro-reflective paint.

The installation of the camera pair on the test rig for stereoscopic IPCT measurements is shown in Fig. 13. The cameras are about 2 m distant from the blades and are mounted on a support that is decoupled from the rig to prevent vibration issues.

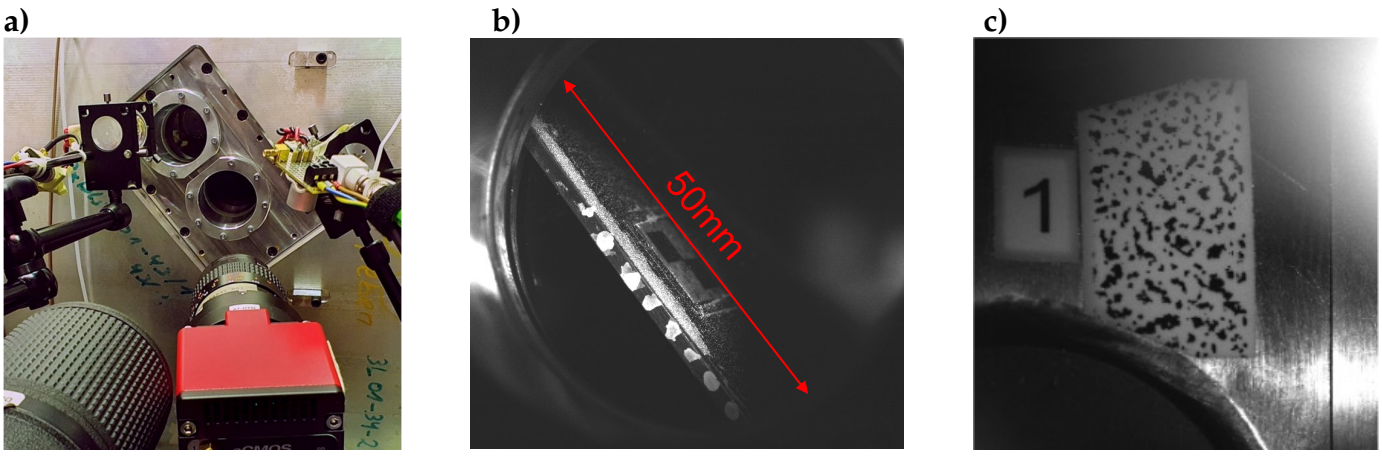

Figure 10. Setup for simultaneous imaging of blade-tip and reference marker on hub (**a**); captured image of the blade tip with painted reference markers (**b**) and corresponding image of the hub reference marker (**c**), both recorded with a HP-LED pulse of 1 µm duration.

During the actual measurement campaign, image sequences were acquired simultaneously with all four cameras at 65, 85 and 95% of the design speed on the working line and additionally under throttled conditions at 65% and 85%. Image recordings of the markers at rotor standstill served as reference (i.e., first frame in dual frame cross-correlation analysis). Before measurements at a specific rotational speed, the angular position of the blade was adjusted to match the reference image as closely as possible by adjusting the phase angle using contrast minimization in the online difference image. At each operating point, a full circumferential traverse of the boundary layer fence was performed over 0°–342° in steps of 18°. Except at 95% speed, the radial penetration depth of the boundary layer fence was 120 mm, at the largest measured speed it was 70 mm. At each angle of the boundary layer fence 750 frames were recorded per camera ($4 \times 20 \times 750$ images per sequence). For reference, additional image sequences of 1000–3000 images were recorded at clean conditions (fence retracted) for each operation condition and at very low aerodynamic load (15% of the design speed).

3.3. Evaluation of tip displacements

In a further step, the displacements at the blade tip were evaluated in relation to the hub displacements near the blade foot which can later be used for an assessment of stereoscopic IPCT evaluations.

To enhance the pattern contrast and to compensate for spatial variations of illumination, images are high pass filtered by a Gaussian kernel of more than twice the width of the largest structure of the speckle pattern. Images of the hub camera were binarized additionally to further enhance contrast. Due to this pre-processing, the standard deviation of hub displacements within a field of 3×5 vectors covering the marker in Fig. 10c was reduced to < 0.05 pixels (< 1.1 µm). For further processing, the instantaneous hub displacement was extracted based on the average of the 3×3 central displacement vectors of the speckle pattern on the hub.

In order to recover the instantaneous deformation vectors at the blade tip and to reject simultaneous displacement components resulting from deviations of the angular reference position, the frame-to-frame jitter as well as torsion and vibration of the rotor drive shaft, image displacements evaluated near the blade foot are subtracted from tip displacements. Before subtraction, circumferential hub displacements in the direction of rotation are balanced with the radius ratio (r_{tip}/r_{hub}).

During an angular traverse, blade tip displacements of up to 280 pixels occurred relative to the reference position. Thus, prior to cross-correlation analysis, images were shifted by a integer offset determined from the mean image of each recorded sequence.

Mean displacements obtained from 3000 individual shots are shown in Fig. 11a, for 42% of design speed (working line) with respect to idle conditions at 15%. The vector diagram clearly shows a shift of the blade tip from the pressure to the suction side at this moderate speed increase. With a further significant increase of the speed to 85%, increasing centrifugal forces lead to a straightening of the composite fan blade resulting in a significant displacement of the blade tip in the direction of rotation as clearly visible in the vector plot in Fig. 11b.

3.4. Tip displacements induced by the BLI

Fig. 12 shows displacements extracted from the center position of the blade tip (c.f. colored vector in Fig. 11b) for two speeds (both points lay on the working line) and phase averaged on each angular position of the boundary layer fence. Without BLI (red circle), the blade tip of R1 undergoes an increasing upstream deflection when the speed changes from 65% to 85%, with the circumferential displacement almost doubling in amplitude. With BLI (black line) a clear modulation of the blade tip deflection with local maxima and minima can be observed which results from the superposition of the bending and possibly also torsional modes of the blades. Assuming aeroelastic equality of the blades and neglecting possible orbiting of the shaft, these results can be considered as the dynamic aeroelastic response of R1 to the BLI within one revolution. Although the angular distribution of the axial displacements (c.f. Fig. 12a and b) shows larger variations in the interval 315°–90°, a positive phase shift in the direction of rotation of the rotor of about 20° can be recognized with increase of the rotational speed (e.g. the local maximum at 270° in subplot a shifts to 290° in subplot b). The same phase shift can be seen for the circumferential displacements (between the subplots c and d): the plateau 110°–250° shifts to 130°–270°. This phase shift is probably related to the different propagation velocities of the disturbance at different inlet Mach numbers

and the increase in rotational speed, which causes a phase shift of similar deflections, assuming a similar response time. Deeper aeroelastic analyses and comparisons with numerical simulations are part of future research work.

3.5. Stereo IPCT measurements

Stereoscopic imagery of the blades was recorded synchronously with the blade-tip measurements for all measurement conditions, but have not been analyzed at the time of writing. For the measurements a pair of sCMOS cameras (ILA.PIV.sCMOS, 2540×2048 pixel) with 105 mm lenses (Nikon Micro Nikkor 105/2.8) observed the blade's surface from a distance of about 2 m through two large plane windows upstream of the fan stage (c.f. Fig. 13a). HP-LEDs as used for the blade tip measurements were placed close to the optical axis of the lenses provided the necessary stroboscopic illumination. This placement ensured optimal backscattering signal of the retro-reflective paint sprayed onto the blade's surface.

Figure 14 shows maps of the in-plane blade displacement for each camera calculated from a single image pair acquired at the 85% speed-line with respect to an idle condition at 15% speed. Processing was performed using standard 2d-2c cross-correlation PIV software (PIVview3.9, PIVTEC GmbH) using sample windows of 64×64 pixels on a coarse-to-fine scheme. While not reconstructed in 3d, displacements exceeding 30 pixels indicate considerable blade deformation. In order to reconstruct the 3d deformation, modifications to the currently available IPCT processing software is necessary in order to accommodate the highly 3d contour of the blade. This is subject of ongoing efforts.

4. Conclusions

Blade deformation measurements could be realized on a highly loaded double-rotor fan rig with composite blades. The simultaneous measurement of both hub and blade tip accounted both for trigger jitter as well as torsion and vibration of the spindle driving the rotor. Modifications to pulsed high-current drivers improved the rise-time of the light emission of the HP-LEDs to considerably shortened the effective light pulse and thereby reducing the motion blur of the rotating blades. The use of retro-reflective paint containing small glass spheres as a coating for the rotor blades provided superior signal in comparison to the traditionally used marker-based pattern. Beyond this, this retro-reflective coating was easily applied with a spray can and could later be removed with alcohol-based solvent.

While yet to be processed the acquired stereo IPCT data is of high quality and can be analysed using conventional correlation-based algorithms. Results from this analysis along with comparisons with numerically predicted blade deformations will be subject of forthcoming publications by the authors.

References

Aulich, A.-L., Görke, D., Blocher, M., Nicke, E., & Kocian, F. (2013). Multidisciplinary automated optimization strategy on a counter rotating fan. In *ASME Turbo Expo 2013.* American Society of Mechanical Engineers (ASME). Retrieved from `https://elib.dlr.de/84484/`

Boden, F., & Stasicki, B. (2014). Non-intrusive in-flight propeller blade deformation measurements by means of a rotating camera. In *ETC2014 - 34. European Telemetry and Test Conference, nürnberg, 03-05 june 2014* (p. 58 - 63). DOI: 10.5162/etc2014/4.1

Halbritter, H., Jäger, C., Weber, R., Schwind, M., & Möllmer, F. (2014). High-speed LED driver for ns-pulse switching of high-current LEDs. *IEEE Photonics Technology Letters*, *26*(18), 1871-1873. DOI: 10.1109/LPT.2014.2336732

Kirmse, T., Maring, S., Ebel, P.-B., & Schröder, A. (2016). Fan blade deformation measurements on the DLR Airbus A320-ATRA by means of IPCT as part of the ground test campaign in the frame of the DLR-project SAMURAI. In A. Dillmann, G. Heller, E. Krämer, C. Wagner, & C. Breitsamter (Eds.), *New Results in Numerical and Experimental Fluid Mechanics X* (p. 629-638). Cham: Springer International Publishing. DOI: 10.1007/978-3-319-27279-5_55

Lengyel-Kampmann, T., Karboujian, J., Schnell, R., & Winkelmann, P. (2022). Experimental investigation of an efficient and lightweight designed counter-rotating shrouded fan stage. In *Proceedings 25th ISABE Conference, 25 September 2022, Ottawa, Canada.*

Meyer, R., Kirmse, T., & Boden, F. (2014). Optical in-flight wing deformation measurements with the image pattern correlation technique. In A. Dillmann, G. Heller, E. Krämer, H. Kreplin, W. Nitsche, & U. Rist (Eds.), (Vol. 124). Cham: Springer International Publishing. DOI: 10.1007/978-3-319-03158-3_55

Roesgen, T. (2003). Optimal subpixel interpolation in particle image velocimetry. *Experiments in Fluids*, *35*, 252-256. DOI: 10.1007/s00348-003-0627-8

Schmid, T., Lengyel-Kampmann, T., Schmidt, T., & Nicke, E. (2019). Optimization of a carbon-fiber composite blade of a counter-rotating fan for aircraft engines. In *13th European Conference on Turbomachinery Fluid dynamics & Thermodynamics ETC13.* Lausanne, Switzerland: European Turbomachinery Society. DOI: 10.29008/ETC2019-432

Tsai, R. (1987, August). A versatile camera calibration technique for high-accuracy 3D machine vision metrology using off-the-shelf TV cameras and lenses. *IEEE Journal on Robotics and Automation*, *3*(4), 323–344. DOI: 10.1109/JRA.1987.1087109

Willert, C. (2006). Assessment of camera models for use in planar velocimetry calibration. *Experiments in Fluids*, *41*(1), 135–143. (Publisher: Springer Berlin / Heidelberg) DOI: 10.1007/s00348-006-0165-2

Willert, C., Stasicki, B., Klinner, J., & Moessner, S. (2010, July). Pulsed operation of high-power light emitting diodes for imaging flow velocimetry. *Measurement Science and Technology*, *21*(7), 075402. DOI: 10.1088/0957-0233/21/7/075402

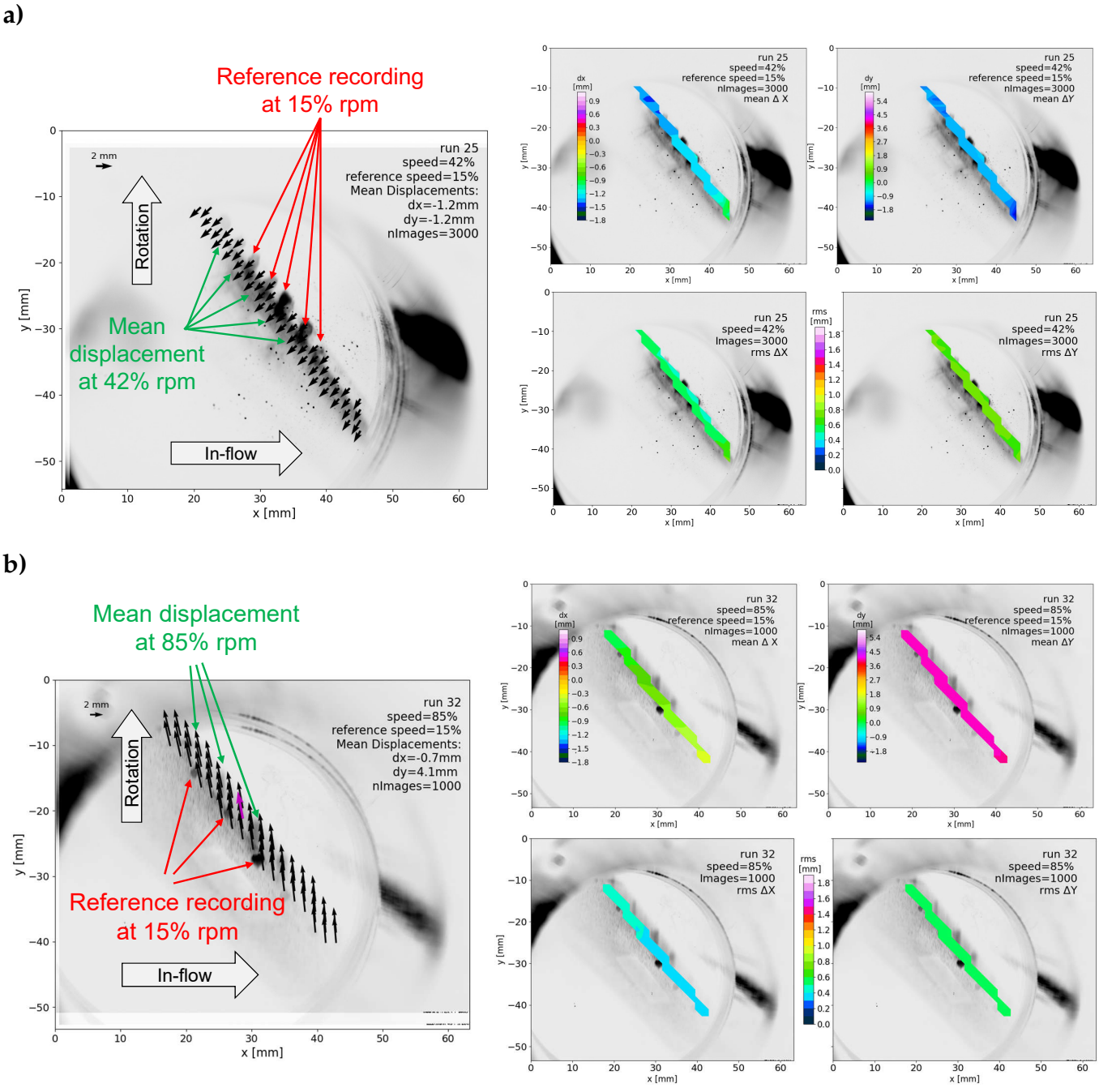

Figure 11. Blade tip displacement data at obtained at clean conditions (boundary layer fence retracted, working line) at the speed-line of 42% (**a**) and 85% (**b**). Image intensities are inverted, i.e. high intensity pixels are white.

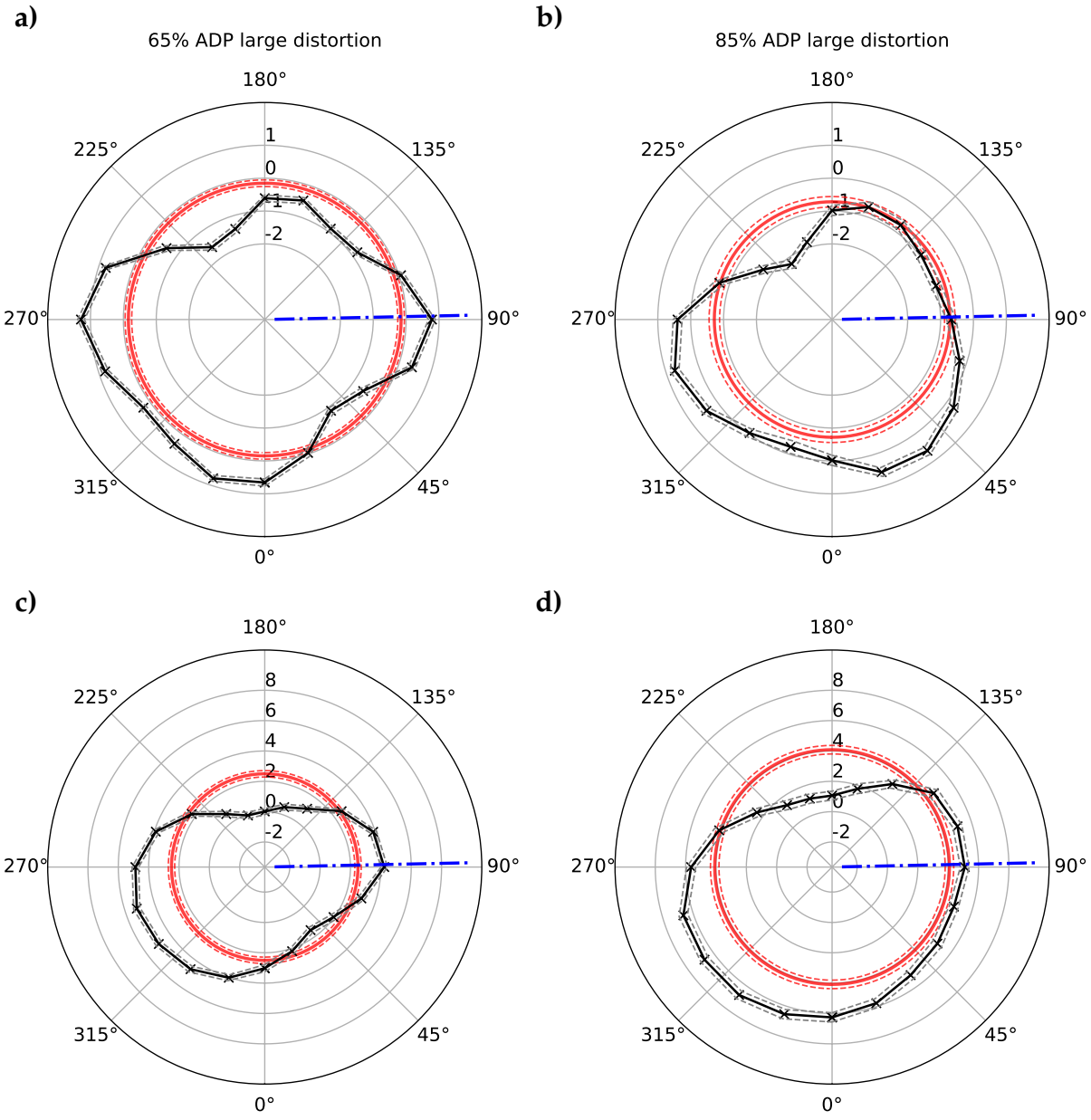

Figure 12. Mean axial (top) and circumferential displacements (bottom) of the centered vector on the blade tip for different angular positions of the upstream flow distortion and for 65% (**a,c**) and 85% (**b,d**) rotational speed. Red circles indicates static blade displacements without flow distortion, that is, with the boundary layer fence retracted. −− ±1 standard deviation of the unsteady displacements; − · −· the angle at which fence angle and the observed blade overlap.(c.f. Fig. 3b)

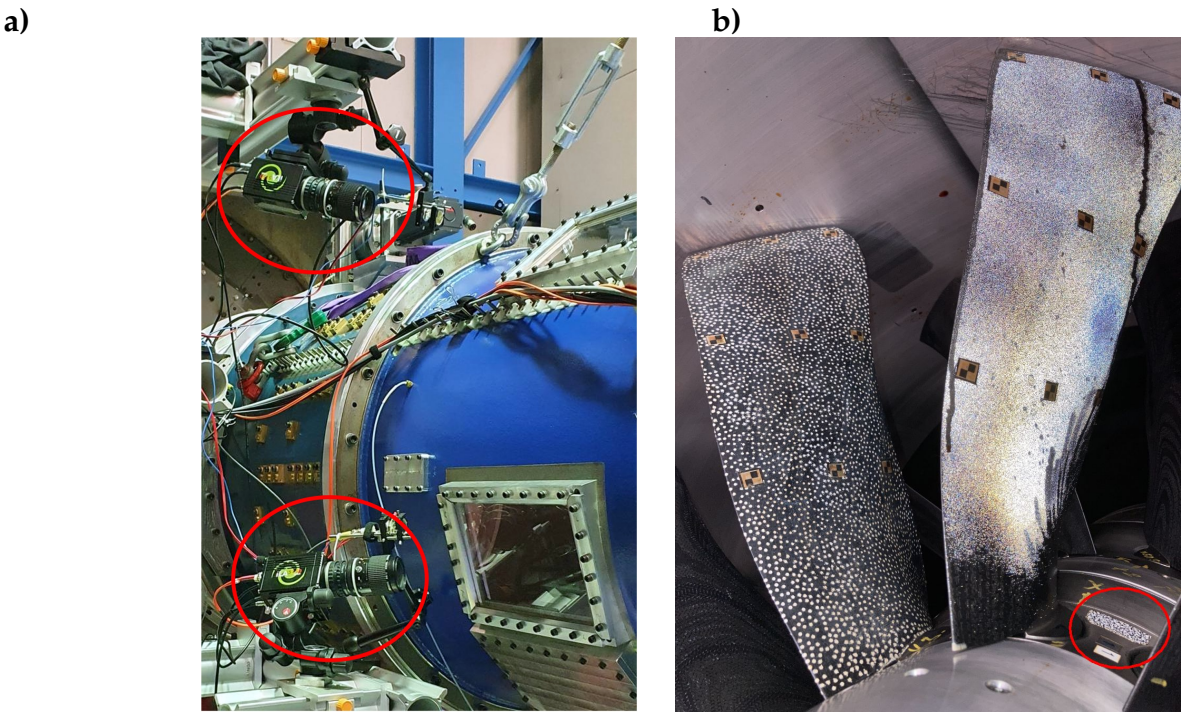

Figure 13. Pair of sCMOS cameras in stereoscopic configuration for imaging the blade deformation with IPCT (**a**). Rotor blades coated with random dot pattern (left blade) and retro-reflecting glass beads (right blade). Red circle indicates reference pattern on rotor hub to obtain absolute reference of the blade's position with respect to the hub (**b**). The black streaks on the right blade are caused by oil leakage from the rotor bearings.

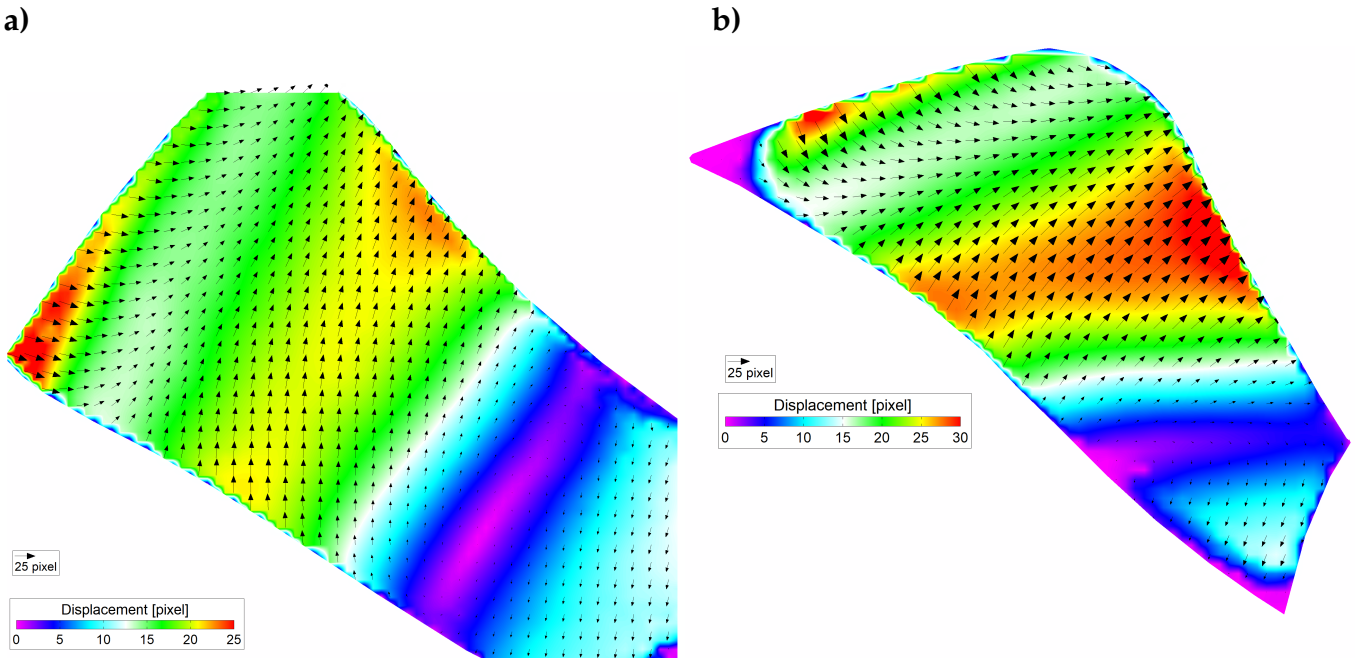

Figure 14. Uncalibrated blade deflection at speed-line 85% with respect unloaded condition at speed-line 15% for camera 1 (**a**) and camera 2 (**b**).